HAL open science

Lagrangian and Eulerian accelerations in turbulent stratified shear flows

Frank G. Jacobitz, Kai Schneider

To cite this version:

Frank G. Jacobitz, Kai Schneider. Lagrangian and Eulerian accelerations in turbulent stratified shear flows. Physical Review Fluids, 2021, 6 (7), 10.1103/PhysRevFluids.6.074609 . hal-03295503

HAL Id: hal-03295503

https://hal.science/hal-03295503v1

Submitted on 25 Sep 2023

HAL is a multi-disciplinary open access archive for the deposit and dissemination of scientific research documents, whether they are published or not. The documents may come from teaching and research institutions in France or abroad, or from public or private research centers.

L'archive ouverte pluridisciplinaire **HAL**, est destinée au dépôt et à la diffusion de documents scientifiques de niveau recherche, publiés ou non, émanant des établissements d'enseignement et de recherche français ou étrangers, des laboratoires publics ou privés.

Submitted to Physical Review Fluids

Lagrangian and Eulerian Accelerations in Turbulent Stratified Shear Flows

Frank G. Jacobitz[1,*] and Kai Schneider[2,†]

[1] *Mechanical Engineering Department,*
Shiley-Marcos School of Engineering, University of San Diego,
5998 Alcalá Park, San Diego, CA 92110, USA

[2] *Aix-Marseille Université, CNRS, Centrale Marseille,*
Institut de Mathématiques de Marseille (I2M),
39 rue Joliot-Curie, 13453 Marseille Cedex 13, France

(Dated: July 22, 2021)

arXiv:2107.10221v1 [physics.flu-dyn] 21 Jul 2021

Abstract

The Lagrangian and Eulerian acceleration properties of fluid particles in homogeneous turbulence with uniform shear and uniform stable stratification are studied using direct numerical simulations. The Richardson number is varied from $Ri = 0$, corresponding to unstratified shear flow, to $Ri = 1$, corresponding to strongly stratified shear flow. The probability density functions (pdfs) of both Lagrangian and Eulerian accelerations have a stretched-exponential shape and they show a strong and similar influence on the Richardson number. The extreme values of the Eulerian acceleration are stronger than those observed for the Lagrangian acceleration. Geometrical statistics explain that the magnitude of the Eulerian acceleration is larger than its Lagrangian counterpart due to the mutual cancellation of the Eulerian and convective acceleration, as both vectors statistically show an anti-parallel preference. A wavelet-based scale-dependent decomposition of the Lagrangian and Eulerian accelerations is performed. The tails of the acceleration pdfs grow heavier for smaller scales of turbulent motion. Hence the flatness increases with decreasing scale, indicating stronger intermittency at smaller scales. The joint pdfs of the Lagrangian and Eulerian accelerations indicate a trend to stronger correlations with increasing Richardson number and at larger scales of the turbulent motion. A consideration of the terms in the Navier–Stokes equation shows that the Lagrangian acceleration is mainly determined by the pressure-gradient term, while the Eulerian acceleration is dominated by the nonlinear convection term. A similar analysis is performed for the Lagrangian and Eulerian time-rates of change of both fluctuating density and vorticity. The Eulerian time-rates of change are observed to have substantially larger extreme values than those of their Lagrangian counterparts due to the the advection terms in the advection-diffusion equation for fluctuating density and in the vorticity equation, respectively. The Lagrangian time-rate of change of fluctuating vorticity is mainly determined by the vortex stretching and tilting term in the vorticity equation. Since the advection-diffusion equation for fluctuating density lacks a quadratic term, the Lagrangian time-rate of change pdfs of fluctuating density show a more Gaussian shape, in particular for large Richardson numbers. Hence, the Lagrangian acceleration and time-rates of change of fluctuating density and vorticity reflect the dominant physics of the underlying governing equations, while the Eulerian acceleration and time-rates of change are mainly determined by advection.

PACS numbers: 47.27.Ak, 47.27.E-, 47.27.ek, 47.27.er, 47.27.Gs

* jacobitz@sandiego.edu

† kai.schneider@univ-amu.fr

I. INTRODUCTION

An understanding of the Lagrangian acceleration properties of a fluid particle in turbulent motion is of fundamental importance and numerous applications exist in geophysical, environmental, and engineering flows. It aids in the study of transport and mixing, as well as in the characterization of geometric properties and intermittency at various scales of turbulent motion. As proposed in Tsinober *et al.* [1] and Tsinober [2], the Lagrangian description of turbulent flows may be a more natural approach to the study of turbulence, as it is more directly related to the dynamics of fluid particles, which are subjected to different forces, e.g., due to the fluctuating pressure gradient, buoyancy, viscous stresses, or other forcing terms.

Studying Lagrangian acceleration has some history. After early work by Heisenberg [3] and Yaglom [4], more recent studies range from theoretical investigations (e.g. Tsinober *et al.* [1], Tsinober [2]) to applications such as the modeling of particle dispersion (e.g. Pope [5]) highly relevant to turbulent combustion. Such studies are carried out using both experimental (e.g. La Porta *et al.* [6]) as well as computational (e.g. Yeung and Pope [7], Yeung [8] or Toschi and Bodenschatz [9]) approaches.

The majority of previous investigations focused on Lagrangian properties of isotropic turbulence. The Lagrangian acceleration was found to be strongly intermittent and heavy tails were observed in its probability density functions (pdf). For example, extreme values as high as 1,500 times the acceleration of gravity were observed for the Lagrangian acceleration of fluid particles by La Porta *et al.* [6] and numerical simulations by Toschi and Bodenschatz [9] confirmed these results.

Acceleration fluctuations and the different contributions have been studied in Tsinober *et al.* [1], Pinsky *et al.* [10] in isotropic turbulence. Their work is motivated by the random Taylor hypothesis or sweeping decorrelation hypothesis stating that 'small eddies in turbulent flow being swept past a stationary Eulerian observer' [1]. It is based on the prediction of Tennekes [11] that states that the Lagrangian acceleration must be small, justified by considering Eulerian and Lagrangian time scales. He predicted that the rms value of the Lagrangian acceleration is a factor $Re_\lambda^{-1/2}$ smaller than the Eulerian value. Lin [12] showed that there is no general justification to extend Taylor's hypothesis to turbulent shear flow. He gives some perspectives that this may still hold for large wavenumbers (small scales),

which will be the topic of future work.

In Tsinober *et al.* [1] direct numerical simulation data of isotropic turbulence were analyzed for different Reynolds numbers and the Lagrangian acceleration, called total acceleration in Tsinober's work, was decomposed into the Eulerian acceleration (called local acceleration in [1]) and the convective contribution. Possible cancellation properties between the Eulerian and convective contributions may yield reduced values of the Lagrangian acceleration. The authors found that the variance of Lagrangian acceleration is much smaller than the Eulerian (local) acceleration and the advection term due to their strong negative alignment (or correlation) for sufficiently high R_λ, here 140. They also observed that the Lagrangian acceleration is strongly correlated with the pressure gradient. Their results are thus in support with the random Taylor hypothesis.

Note that the convective contribution of the acceleration becomes large when the flow is non-uniform, i.e., if the velocity changes along a streamline. The convective acceleration term is nonlinear, which causes mathematical difficulties in flow analysis; also, even in steady flow (which is perfect for Taylor's hypothesis), the convective acceleration can be large if spatial gradients of velocity are large. In case it is anti-aligned with the local acceleration, it can be balanced and the total acceleration can still be small. This implies that the rate of Eulerian decorrelation is higher than that of Lagrangian decorrelation, which is crucial for two-point closures, see also the review on space-time correlations in turbulence by He *et al.* [13].

Many applications of Lagrangian dynamics target the transport and mixing of natural and anthropogenic substances in the geophysical environment. Such flows are often characterized by the presence of shear and stratification. Homogeneous turbulent stratified shear flows with constant vertical stratification rate $S_\rho = \partial\varrho/\partial y$ and constant vertical shear rate $S = \partial U/\partial y$ represents the simplest flow configuration in order to study the competing effects of shear and stratification. This flow has been investigated extensively in the past. Experimental studies include work by Komori *et al.* [14], Rohr *et al.* [15], Piccirillo and Van Atta [16], and Keller and Van Atta [17]. Numerical simulations were performed by Gerz *et al.* [18], Holt *et al.* [19], Jacobitz *et al.* [20], Jacobitz [21], and Portwood [22]. Hanazaki and Hunt [23] analyzed this flow using linear theory. More recently, the mixing properties of turbulent stratified shear flow have been considered by, for example, Salehipour *et al.* [24] and Venayagamoorthy and Koseff [25]. For a review, we refer to Gregg *et al.* [26].

More recently, Jacobitz *et al.* [27] considered Lagrangian and Eulerian accelerations in rotating and sheared homogeneous turbulence. It was found that the Lagrangian acceleration was mainly determined by the pressure-gradient term in the Navier–Stokes equation, while the Eulerian acceleration shows stronger tails due to the advection term. In the case of strong rotation, linear effects are dominant and the Lagrangian acceleration pdf takes an approximately Gaussian shape. A comparison of linear theory with direct numerical simulation of rotating and sheared homogeneous turbulence was performed by Salhi *et al.* [28].

The goal of this work is to investigate the acceleration statistics and to analyze the different contributions to the acceleration in turbulent stratified shear flows using direct numerical simulations. A key question is the understanding of the properties of Lagrangian acceleration fluctuations and their Eulerian counterpart and the influence of the Richardson number.

In the following, the numerical approach taken in this study is introduced first. Then the Richardson number dependence of the Lagrangian and Eulerian acceleration pdfs are presented and geometrical statistics of the alignment angles of the different contributions. Using a wavelet-based scale-dependent decomposition, the Lagrangian and Eulerian accelerations are studied at various scales of the turbulent motion and their spatial fluctuations are analyzed. The corresponding Lagrangian and Eulerian time-rates of change pdfs for the fluctuating density are discussed. Finally, a summary and conclusion of the present work is provided. Results for the Lagrangian and Eulerian time-rates of change for the fluctuating vorticity as well as the Lagrangian and Eulerian acceleration component are discussed in the appendix.

II. APPROACH

In this section, the equations of motion and their direct numerical solution are described, variance estimates for the Lagrangian and Eulerian accelerations are given, the wavelet-based scale-dependent decomposition of the accelerations is introduced, and geometrical statistics to study the alignment of the different acceleration contributions are motivated.

A. Equations of Motion

The mean flow with velocity (U, V, W) and density ϱ considered in this study has a constant vertical shear rate $S = \partial U/\partial y$ and a constant vertical stratification rate $S_\rho = \partial \varrho/\partial y$, respectively:

$$U = Sy, \qquad V = W = 0, \qquad \varrho = \rho_0 + S_\rho y, \tag{1}$$

where ρ_0 is the ambient density.

This study is based on the incompressible Navier–Stokes equations for the fluctuating velocity and an advection-diffusion equation for the fluctuating density:

$$\nabla \cdot \boldsymbol{u} = 0 \tag{2}$$

$$\begin{aligned} &\frac{\partial \boldsymbol{u}}{\partial t} + \boldsymbol{u} \cdot \nabla \boldsymbol{u} + Sy\frac{\partial \boldsymbol{u}}{\partial x} + Sv\boldsymbol{e}_x \\ &\quad = -\frac{1}{\rho_0}\nabla p - \frac{g}{\rho_0}\rho \boldsymbol{e}_y + \nu \nabla^2 \boldsymbol{u} \end{aligned} \tag{3}$$

$$\frac{\partial \rho}{\partial t} + \boldsymbol{u} \cdot \nabla \rho + S_\rho v = \alpha \nabla^2 \rho \tag{4}$$

Here, $\boldsymbol{u} = (u, v, w)$ is the fluctuating velocity, p the fluctuating pressure, ρ the fluctuating density, ν the kinematic viscosity, and α the scalar diffusivity. Taking the curl of the momentum equation (3) leads to the vorticity equation:

$$\begin{aligned} &\frac{\partial \boldsymbol{\omega}}{\partial t} + \boldsymbol{u} \cdot \nabla \boldsymbol{\omega} + \nabla \times \left(Sy\frac{\partial \boldsymbol{u}}{\partial x} + Sv\boldsymbol{e}_x \right) \\ &\quad = \boldsymbol{\omega} \cdot \nabla \boldsymbol{u} - \nabla \times \left(\frac{g}{\rho_0}\rho \boldsymbol{e}_y \right) + \nu \nabla^2 \boldsymbol{\omega} \end{aligned} \tag{5}$$

B. Numerical Approach

For their numerical solution, the equations of motion (2-4) are transformed into a frame of reference moving with the mean velocity (see Rogallo [29]). This transformation enables the application of periodic boundary conditions for the fluctuating components of velocity and density. A spectral collocation method is used for the spatial discretization and the solution is advanced in time with a fourth-order Runge–Kutta scheme.

Table I provides an overview of the simulations performed for this study. The Richardson number $Ri = N^2/S^2$ is varied from $Ri = 0$, corresponding to unstratified shear flow, to

$Ri = 1$, corresponding to strongly stratified shear flow. While both the mean shear rate $S = \partial U/\partial y$ and the mean stratification rate $S_\rho = \partial \varrho/\partial y$ are constant for a given simulation, the Richardson number variation is obtained by a change of the Brunt–Väisälä frequency N with $N^2 = -g/\rho_0 S_\rho$, while keeping the mean shear rate S constant.

The initial conditions are taken from a separate simulation of isotropic turbulence without density fluctuations, which was allowed to develop for approximately one eddy turnover time. The initial values of the Taylor-microscale Reynolds number $Re_\lambda q\lambda/\nu = 89$ and the shear number $SK/\epsilon = 2$ are fixed. Here q is the rms of the fluctuating velocity with $q^2 = \overline{u_i u_i}$, λ the Taylor-microscale with $\lambda^2 = 5q^2\nu/\epsilon$, $K = q^2/2$ the kinetic energy, and $\epsilon = \nu\overline{\partial u_j/\partial x_k \partial u_j/\partial x_k}$ the dissipation rate.

Table I provides an overview of the eventual values of Re_λ, q, and ϵ at time $St = 10$. The table also lists values of a variety of length scales, including the overturning scale $L_{overturn} = q^3/\epsilon$, the Ellison scale $L_{Ellison} = \rho/S_\rho$, the Ozmidov scale $L_{Ozmidov}$ with $L^2_{Ozmidov} = \epsilon/N^3$, the Taylor-microscale λ, and the Kolmogorov scale η with $\eta^4 = \nu^3/\epsilon$, indicating an appropriate resolution of the simulations at $St = 10$ at both the large and small scales of the turbulent motion.

The simulations are performed on a parallel computer using $512 \times 512 \times 512$ grid points. To increase the resolution, instead of the classical dealiasing with a cut-off at 2/3 of the maximum wavenumber, a cosine-filter dealiasing is applied. The cosine-filter is only applied to wavenumbers larger than 2/3 of the maximum wavenumber. Its transfer function starts with one at 2/3 of the maximum wavenumber, goes to zero at the maximum wavenumber, and it follows the shape of the first quarter of the cosine function period. The maximum wavenumber k_{max} can be defined when the cosine is equal to the value 1/2. For the current resolution with $N = 512$ we thus have $k_{max} = 227$ (instead of the value 170 obtained for classical dealiasing). All simulations are well resolved and we have $k_{max}\eta > 1.2$ in the eventual evolution for the unstratified case. A discussion on the influence of dealising in pseudo-spectral codes can be found in Hou and Li [30]. The authors show that the classical 2/3 rule does not necessarily yield the best results and other filtering techniques, different from the cosine-dealiasing used here, are more efficient, supporting our choice.

C. Variance Estimates for the Lagrangian and Eulerian Accelerations in Stratified Shear Flow

The Lagrangian and Eulerian accelerations are defined as

$$\boldsymbol{a}_L = \frac{\partial \boldsymbol{u}}{\partial t} + \boldsymbol{u} \cdot \nabla \boldsymbol{u} \quad \text{and} \quad \boldsymbol{a}_E = \frac{\partial \boldsymbol{u}}{\partial t}, \tag{6}$$

respectively. Both accelerations are computed as a volume average at a fixed time, which is an appropriate choice for homogeneous flows. The effects of shear and buoyancy are considered as external forces.

In [27] we provided estimates of the variances of the Lagrangian and Eulerian accelerations writing the Navier–Stokes equations in the form

$$\frac{\partial \boldsymbol{u}}{\partial t} = -\boldsymbol{N} - \boldsymbol{\Pi} - \boldsymbol{\Lambda}, \tag{7}$$

where the terms on the right hand side are given by

$$\begin{aligned} \boldsymbol{N} &= \boldsymbol{a}_C = \boldsymbol{u} \cdot \nabla \boldsymbol{u} \\ \boldsymbol{\Pi} &= \boldsymbol{a}_P = \nabla (p/\rho_0) \\ \boldsymbol{\Lambda} &= \boldsymbol{\Lambda}_S + \boldsymbol{\Lambda}_B + \boldsymbol{\Lambda}_V = Sv\boldsymbol{e}_x + \frac{g}{\rho_0}\rho \boldsymbol{e}_y - \nu \nabla^2 \boldsymbol{u}. \end{aligned} \tag{8}$$

Here, $\boldsymbol{N}$ is the nonlinear or advection term, $\boldsymbol{\Pi}$ the pressure-gradient term, and $\boldsymbol{\Lambda}$ the linear term with contributions from shear, buoyancy, and viscous effects. The notation $\boldsymbol{a}_C$ for the nonlinear term and $\boldsymbol{a}_P$ for the pressure gradient match the notation in Tsinober *et al.* [1] to denote the convective and pressure contributions, respectively, to the accelerations.

According to [27] we have also in the case of stratified shear flow the identity

$$\left\langle \|\boldsymbol{N} + \boldsymbol{\Pi} + \boldsymbol{\Lambda}\|^2 \right\rangle = \left\langle \|\boldsymbol{N} + \boldsymbol{\Lambda}\|^2 \right\rangle - \left\langle \|\boldsymbol{\Pi}\|^2 \right\rangle. \tag{9}$$

Here, $\|\cdot\|$ denotes the magnitude of a vector and $\langle \cdot \rangle$ the volume average for a homogeneous field.

This directly implies the following exact identities for the variances of the Eulerian acceleration $\boldsymbol{a}_E$ (called local acceleration in Tsinober *et al.* [1]),

$$a_E^2 \equiv \left\langle \|\frac{\partial \boldsymbol{u}}{\partial t}\|^2 \right\rangle = \left\langle \|\boldsymbol{N} + \boldsymbol{\Pi} + \boldsymbol{\Lambda}\|^2 \right\rangle = \left\langle \|\boldsymbol{N} + \boldsymbol{\Lambda}\|^2 \right\rangle - \left\langle \|\boldsymbol{\Pi}\|^2 \right\rangle \tag{10}$$

and of the Lagrangian acceleration $\boldsymbol{a}_L$ (called total acceleration in Tsinober *et al.* [1]),

$$a_L^2 \equiv \left\langle \|\frac{\partial \boldsymbol{u}}{\partial t} + \boldsymbol{u}\cdot\nabla\boldsymbol{u}\|^2 \right\rangle = \left\langle \|\boldsymbol{\Pi} + \boldsymbol{\Lambda}\|^2 \right\rangle . \tag{11}$$

The variance estimates provided in [27] for rotating shear flows are now extended to stratified shear flows, again with the underlying assumption and crucial simplification of isotropy of the flow. The main difference arises in the linear term $\boldsymbol{\Lambda}$, which now includes a buoyancy force, instead of a Coriolis force. Neglecting the friction force, the variance of the linear term can be written as

$$\Lambda^2 = \frac{1}{3}S^2[1 + 3(\frac{g}{\rho_0})^2\frac{1}{S^2}\frac{\rho^2}{u^2}]u^2. \tag{12}$$

Using the ratio of potential to kinetic energy

$$\frac{K_\rho}{K} = \frac{-\frac{1}{2}\frac{g}{\rho_0}\frac{\rho^2}{S_\rho}}{\frac{1}{2}u^2} = -\frac{g}{\rho_0}\frac{1}{S_\rho}\frac{\rho^2}{u^2} \tag{13}$$

the variance for the linear term can be written as

$$\Lambda^2 = \frac{1}{3}S^2[1 + 3Ri\frac{K_\rho}{K}]u^2. \tag{14}$$

Hence, the variance estimate of the linear term retains the ratio of potential to kinetic energy.

D. Scale-dependent decomposition of Lagrangian and Eulerian accelerations

To gain insight into the scale dependence of the Lagrangian and Eulerian accelerations, we decompose both accelerations into an orthogonal wavelet series. Wavelets are well localized functions in space and in scale (or wave number), see e.g. [31], and different wavelet-based diagnostics, including the scale-dependent energy distribution and its spatial fluctuations, intermittency measures such as the scale dependent flatness and anisotropy measures, have been proposed. For a review we refer the reader to [32].

We consider a generic vector field $\boldsymbol{a} = (a_1, a_2, a_3)$ at a fixed time instant and decompose each component $a_\alpha(\boldsymbol{x})$ into an orthogonal wavelet series,

$$a_\alpha(\boldsymbol{x}) \;=\; \sum_\lambda \widetilde{a}^\alpha_\lambda\, \psi_\lambda(\boldsymbol{x}), \tag{15}$$

where the wavelet coefficients are given by the scalar product $\widetilde{a}^\alpha = \langle a_\alpha, \psi_\lambda\rangle$. The wavelets ψ_λ with the multi-index $\lambda = (j, \boldsymbol{i}, d)$ are well localized in scale $L_0 2^{-j}$ (where L_0 corresponds

to the size of the computational domain), around position $L_0\boldsymbol{i}/2^j$, and orientated in one of the seven directions $d = 1, ..., 7$, respectively. The scale is directly related to the wave number $k_j = k_0 2^j$, where k_0 is the centroid wave number of the chosen wavelet family. For Coiflets 12 wavelets used in the present work we have $k_0 = 0.77$. Large scales correspond to small values of the scale index j and to a well localized wavelet in Fourier space around wavenumber k_j. In contrast for small scales, which correspond to large values of j, the wavelet becomes less localized in Fourier space around the mean wavenumber k_j.

Reconstructing the three components a^α at scale 2^{-j} by summing only over the position $\boldsymbol{i}$ and direction d indices in eq. 15 yields the acceleration $\boldsymbol{a}^j$ at scale intex j. In terms of filtering the acceleration at a given scale corresponds to a bandpass filtered field, with a bandpass filter having constant relative bandwidth. This means that the filterwidth becomes larger at larger wavenumber, corresponding to decreasing scale. By construction we have $\boldsymbol{a} = \sum_j \boldsymbol{a}^j$, where the $\boldsymbol{a}^j$ are mutually orthogonal.

The scale-dependent moments, including scale-dependent flatness, and scale-dependent pdfs, can thus be computed from $\boldsymbol{a}^j$ using classical statistical estimators.

For instance the q-th order moment of $\boldsymbol{a}^j(\boldsymbol{x})$ can be defined by,

$$M_q[\boldsymbol{a}^j] = \langle (\boldsymbol{a}^j)^q \rangle, \tag{16}$$

and by construction the mean value vanishes, $\langle \boldsymbol{a}^j \rangle = 0$. The moments are thus central moments. These scale-dependent moments are directly related to the q-th order structure functions [33] where the increment size is $\propto 2^{-j}$.

The scale-dependent flatness, which measures the intermittency of $\boldsymbol{a}^j$ at scale 2^{-j}, is defined by

$$Fl[\boldsymbol{a}^j] = \frac{M_4[\boldsymbol{a}^j]}{(M_2[\boldsymbol{a}^j])^2}. \tag{17}$$

For a Gaussian distribution the flatness equals three at all scales.

E. Geometrical statistics

To understand the magnitude of Eulerian and Lagrangian accelerations, we statistically assess, following Tsinober *et al.* [1], the alignment properties of $\boldsymbol{a}_E$, $\boldsymbol{a}_C = \boldsymbol{N}$ and its sum corresponding to the Lagrangian acceleration $\boldsymbol{a}_L = \boldsymbol{a}_E + \boldsymbol{a}_C$. For convenience, we partly use the notation introduced in [1] in this section. When the vectors of the Eulerian acceleration

$\boldsymbol{a}_E$ and the convective terms $\boldsymbol{a}_C$ are anti-parallel, then the magnitude of the Lagrangian acceleration $\boldsymbol{a}_L$, is small compared to those of the Eulerian and convective contribution, since

$$\langle \boldsymbol{a}_L \boldsymbol{a}_L \rangle = \langle \boldsymbol{a}_E + \boldsymbol{a}_C, \boldsymbol{a}_E + \boldsymbol{a}_C \rangle = \langle \boldsymbol{a}_E, \boldsymbol{a}_E \rangle + \langle \boldsymbol{a}_C, \boldsymbol{a}_C \rangle + 2\cos(\boldsymbol{a}_E, \boldsymbol{a}_C)\, ||\boldsymbol{a}_E||\, ||\boldsymbol{a}_C||. \quad (18)$$

If $\boldsymbol{a}_E$ and $\boldsymbol{a}_C$ are anti-aligned the cosine is negative and the norm of $\boldsymbol{a}_E + \boldsymbol{a}_C$ is minimal. To verify the random Taylor-hypothesis Tsinober *et al.* [1] computed the cosine of the angle of the Eulerian acceleration and the convective term, motivated by the prediction of Tennekes [11] that the Lagrangian acceleration must be small so that the hypothesis holds. We expect this result to hold with modification due to shear and stratification.

For the pressure gradient term $\boldsymbol{a}_P = \boldsymbol{\Pi}$, the alignment with the Eulerian and Lagrangian acceleration can be likewise assessed. For sufficiently high Reynolds numbers we anticipate a strong anti-alignment of $\boldsymbol{a}_P$ with $\boldsymbol{a}_L$ showing that the flow is driven by the pressure gradients and that linear effects are negligible. However, buoyancy may change this result for strong stratification and its impact will be assessed using the simulation results.

For Gaussian divergence free random fields Tsinober *et al.* [1] found similar alignment properties and they concluded that the cancellation of $\boldsymbol{a}_E$ and $\boldsymbol{a}_C$ is mostly a kinematic effect and not due to Navier–Stokes dynamics. A justification for these findings is given by Millionshchikow's zero-fourth cumulant hypothesis [34] which decomposes fourth order moments into a series of second order moments.

III. RESULTS

In this section, the flow evolution is briefly described first. Then, results for the probability density functions (pdfs) of the Lagrangian and Eulerian accelerations are provided, related to the remaining terms in the Navier–Stokes equations, and their scale-dependent properties are presented. A similar analysis is performed for the Lagrangian and Eulerian time-rates of change of fluctuating density and in appendix A also for fluctuating vorticity. In the following, the accelerations and time-rates of change are analyzed at the instant $St = 10$. Table I provides an overview of the series of five simulations performed.

A. Turbulence Evolution

In order to provide a context for the present study, the energetics of the flow is briefly discussed. More details on turbulent stratified shear flows can be found in [20] and [21].

Figure 1 (left) shows the evolution of the turbulent kinetic energy normalized by its initial value K/K_0. All cases result in an initial decay phase due to the isotropic initial conditions. Then, as the Richardson number Ri is increased, the eventual evolution of the turbulent kinetic energy changes from growth to decay with a critical value of $Ri_{cr} \approx 0.15$.

The normalized transport equation for the turbulent kinetic energy evolution can be written as:

$$\gamma = \frac{1}{SK}\frac{dK}{dt} = \frac{P}{SK} - \frac{B}{SK} - \frac{\epsilon}{SK} \tag{19}$$

Here, γ is the growth rate of the turbulent kinetic energy, $P/(SK)$ is the normalized production term with $P = -S\overline{u_1 u_2}$, $B/(SK)$ is the normalized buoyancy flux with $B = g/\rho_0 \overline{u_2 \rho}$, and $\epsilon/(SK)$ is the normalized dissipation rate.

Figure 1 (right) shows the dependence of $P/(SK)$, $B/(SK)$, $\epsilon/(SK)$, and γ on the Richardson number Ri at nondimensional time $St = 10$. The normalized production rate $P/(SK)$ decreases with increasing Richardson number Ri and it assumes a slightly negative value for large Ri cases, indicating a positive Reynolds shear stress (or counter-gradient flux). The normalized buoyancy flux $B/(SK)$ remains relatively small and it converts kinetic to potential energy for most of the Ri range. The normalized dissipation rate $\epsilon/(SK)$ remains relatively unaffected by the Ri variation. The growth rate γ follows the trend of the normalized production rate $P/(SK)$, offset by the contributions of $B/(SK)$ and $\epsilon/(SK)$. Note that positive values of γ correspond to a growth of K, while a negative value of γ indicates decay of the turbulent kinetic energy.

The evolution of the ratio of potential to kinetic energy is given in figure 2 (left). The simulations are initialized without potential energy and a strong initial growth is observed. The ratio of potential to kinetic energy eventually reaches an approximately constant value, which still depends on the Richardson number Ri. This dependence of the ratio K_ρ/K on Ri at nondimensional time $St = 10$ is presented in figure 2 (right). The ratio of K_ρ/K first increases strongly and then reaches a maximum of $K_\rho/K \approx 0.3$ for $Ri = 1$.

B. Lagrangian and Eulerian Accelerations

Figure 3 (top) shows the probability distribution functions (pdfs) of the Lagrangian acceleration $\boldsymbol{a}_L$ (left) and of the Eulerian acceleration $\boldsymbol{a}_E$ (right). The pdfs of both accelerations have stretched-exponential shapes and they exhibit a strong and similar influence on the Richardson number Ri. For small Ri, the extreme values of the Eulerian acceleration are above those of the Lagrangian acceleration, which is consistent with previous observations for sheared and rotating turbulence [27] and likewise observed for isotropic turbulence by Tsinober *et al.* [1].

Figure 3 (bottom) shows the pdfs normalized with the corresponding standard deviations of the two accelerations. For a core region of about five standard deviations, both the Lagrangian and Eulerian accelerations show approximately the same shape. The tails of the pdfs of both accelerations weaken with increasing Ri. For small Ri, the tails of the Lagrangian acceleration are heavier than the tails of the Eulerian acceleration.

Tables II and III provide statistical information of the Lagrangian and Eulerian accelerations as a function of the Richardson number at nondimensional time $St = 10$. The magnitudes (rms values) of both accelerations decrease with increasing Ri and the magnitude of $\boldsymbol{a}_E$ remains always larger than the magnitude of $\boldsymbol{a}_L$, also observed for isotropic turbulence Tsinober *et al.* [1]. At small Ri, the heavier tails observed for the normalized pdfs of $\boldsymbol{a}_L$ as compared to $\boldsymbol{a}_E$ result in a larger flatness of the Lagrangian acceleration pdf as compared to its Eulerian counterpart. The flatness values of both accelerations generally decrease with increasing Ri, indicating a decreased importance of nonlinear effects which is related to the decreasing Reynolds number. However, unlike in the presence of strong rotation considered in [27], the flatness values do not reach a value close to three, characteristic for a Gaussian distribution, in the case of strong stratification. For $Ri = 0$ the flatness values of $\boldsymbol{a}_L$ and $\boldsymbol{a}_E$ are comparable with DNS data of isotropic turbulence [2] at $Re_\lambda = 140$, where the values of 24.4 and 12.8 were found, while we find respectively 27.81 and 14.41 in the case of pure shear. Note that for the variances Tsinober *et al.* [1] found the values (normalized with $\epsilon^{3/2}\nu^{-1/2} = 24.84$, where $\epsilon = 1.20$ and $\nu = 0.0028$) of 2.75 for a_L and 8.19 for a_E (and 10.96 for a_C), while we find respectively the values 8.20 for a_L and 14.81 for a_E (and 22.39 for a_C) in the case of pure shear using the same normalization with $\epsilon^{3/2}\nu^{-1/2}$. This shows that the order is consistent and the values are comparable.

Figure 4 shows pdfs of the shear term (top, left), the buoyancy term (top, right), the pressure-gradient term (bottom, left), and the advection term (bottom, right) in the Navier–Stokes equation. The shear and buoyancy terms depend linearly on fluctuating velocity components and density and their pdfs have hence a Gaussian shape. While the magnitude of the shear term pdf decreases with increasing Ri, the magnitude of the buoyancy term pdf increases. The pdfs of the pressure-gradient and advection terms show a stretched-exponential shape due to the quadratic nature of the terms. The magnitudes of both terms decrease with increasing Ri. For small Ri, the pressure-gradient and advection terms clearly dominate the shear and buoyancy terms, but this dominance somewhat diminishes with increasing Ri. Hence, the pressure-gradient term is the generally dominant contribution to the Lagrangian acceleration, while the advection term is important for the Eulerian acceleration.

Table IV provides the variances of the contributions to the linear term from the shear term Λ_S^2, the buoyancy term Λ_B^2, and the viscous term Λ_V^2. An estimate for the variance of the linear term Λ_{DNS}^2 is computed using the triangle inequality. The table also provides the variance of the velocity q^2, the ratio of potential to kinetic energies K_ρ/K, and a theoretical estimate for the linear term Λ^2 based on equation 14 at nondimensional time $St = 10$. The variances of the linear term computed from the simulation results Λ_{DNS}^2 and the theoretical estimate Λ^2 agree well, despite the assumption of isotropy used in the derivation of equation 14. The variance of the linear term decreases with increasing Richardson number Ri. The Taylor-microscale Reynolds number Re_λ given in table I yields a measure for the general importance of nonlinear effects in a turbulent flow. Re_λ decreases with increasing Ri. The results suggest that nonlinear effects contribute the least to the turbulence evolution for the case with a Richardson number $Ri = 1$.

The joint pdfs of the Lagrangian and Eulerian accelerations are shown in figure 5 for two cases with Richardson numbers $Ri = 0.1$ (left) and $Ri = 1$ (right) at nondimensional time $St = 10$. The correlation between Lagrangian and Eulerian accelerations is observed to increase with increasing Ri. The stronger correlation of the Eulerian and Lagrangian acceleration for $Ri = 1$ is due to the reduced nonlinearity.

In order to quantify this observation, the Pearson product-moment correlation coefficient for the Lagrangian and Eulerian accelerations in dependence of the Richardson number Ri is given in the first line of table V at nondimensional time $St = 10$. For unstratified shear

flow with $Ri = 0$, the Lagrangian and Eulerian accelerations are almost decorrelated as indicated by $r = 0.0284$. With increasing stratification strength, the Pearson product-moment correlation coefficient increases monotonically. A high value of $r = 0.6634$ is observed for $Ri = 1$. This can be explained by the decreasing importance of the nonlinearity, quantified by the decreasing Reynolds number.

To provide further information, geometrical statistics are performed and the vector alignment properties of the different acceleration contributions are studied, as introduced in section II E. For different Richardson numbers we consider the pdf of the cosine of the angle of two acceleration vectors, shown in Figure 6, the mean value of the cosine as quantitative measure and the correlation coefficient, assembled in table V. The choice of the cosine is motivated by the fact that for random fields in 3D the cosine of the angle is uniformly distributed and not the angle itself. Figure 6 (bottom, left) shows that a strong anti-alignment of the Eulerian acceleration $\boldsymbol{a}_E$ and the convective term $\boldsymbol{a}_C = \boldsymbol{N}$ reflected in a peak in the pdf at $\cos = -1$, corresponding to an angle of 180 degrees. This explains why the Lagrangian acceleration is smaller than the Eulerian one and also smaller than the convective term, as the anti-alignment implies that the two vectors $\boldsymbol{a}_E$ and $\boldsymbol{a}_C = \boldsymbol{N}$ are anti-parallel. The Lagrangian acceleration $\boldsymbol{a}_L$ and the pressure gradient $\boldsymbol{\Pi}$ in Fig. 6 (bottom, right) even show a stronger anti-alignment, which confirms that the negative pressure gradient is the driving force of the flow dynamics. In both cases the anti-alignment is most pronounced for $Ri = 0$ and becomes weaker for increasing Richardson numbers. This can be further quantified by mean values of the cosine of the angle and also the correlation coefficient between the two vectors, the results are given in table V.

The Lagrangian acceleration is positively aligned with the Eulerian one (Fig. 6, top, left) and also with the convective acceleration (Fig. 6, top, right). For $\boldsymbol{a}_E$ this alignment becomes stronger with increasing Richardson number, while for $\boldsymbol{a}_C$ this becomes weaker, as the nonlinear term diminishes. These results are consistent with those in Tsinober *et al.* [1] obtained for isotropic turbulence, in the case of $Re_\lambda = 141$ (as compared to our value for unstratified shear flow 157). For example for the average cosine of the angle between a_L and a_E Tsinober *et al.* [1] reports a value 0.105 (for unstratified shear flow we find 0.162), for a_L and a_C 0.353 (0.420) and a_E and a_C -0.762 (-0.657).

Let us also mention that Tsinober *et al.* [1] showed that Gaussian random fields satisfy similar alignment properties for $\boldsymbol{a}_E$ and $\boldsymbol{a}_C = \boldsymbol{N}$ and concluded that this is essentially a

kinematic effect.

Figure 7 presents the scale-dependent pdfs of the Lagrangian acceleration $\boldsymbol{a}_L$ (left) and Eulerian acceleration $\boldsymbol{a}_E$ (right) for two cases with $Ri = 0.1$ (top) and $Ri = 1$ (bottom) at nondimensional time $St = 10$. The pdfs have stretched-exponential shapes and the tails become heavier with increasing scale index j or decreasing scale of the turbulent motion. For the weakly stratified case with $Ri = 0.1$, the tails of the Lagrangian acceleration are generally heavier as those of the Eulerian acceleration. For the strongly stratified case with $Ri = 1$, however, the tails of the Eulerian acceleration are generally heavier than those of their Lagrangian counterpart. This observation reflects the trend for the total acceleration pdfs with increasing Richardson number discussed above.

In order to quantify the above observations, scale-dependent statistics are provided in tables VII and VIII for two cases with Richardson numbers $Ri = 0.1$ and $Ri = 1$, respectively. While the magnitude of the total Eulerian acceleration a_E is larger than the magnitude of the total Lagrangian acceleration a_L, the ordering is reversed for the accelerations at some scales of the turbulent motion. For the case with $Ri = 0.1$, the original ordering holds at the scale with the largest magnitude, which is $j = 6$ for both accelerations. At that scale, the pdfs of the total accelerations are also most similar to the pdfs of the accelerations at that scale. For the case with $Ri = 1$, the ordering observed for the magnitudes of the total accelerations holds more generally at different scales of the turbulent motion. The pdfs of the total accelerations are again most similar at the scales with the largest magnitudes, which are $j = 4$ for the Lagrangian acceleration and $j = 5$ for the Eulerian acceleration. The flatness of the accelerations generally increases with scale index j, indicating more intermittency at the smallest scales of motion. Note that for the Lagrangian acceleration, flatness values close to three are observed for the larger scales with $j = 1$, indicating that the Lagrangian acceleration at large scale is mainly determined by linear effects.

Figure 8 shows the scale-dependent joint pdfs of the Lagrangian and Eulerian accelerations for two cases with $Ri = 0.1$ (left) and $Ri = 1$ (right) as well as at large scale with scale index $j = 3$ (top) and at small scale with $j = 7$ (bottom) at nondimensional time $St = 10$. Consistent with the observation for the total accelerations discussed above, the correlation increases with stratification strength at the two scales shown. In addition, the correlation decreases with increasing scale index j or decreasing scale of the turbulent motion considered.

This observation is shown more quantitatively using the Pearson product-moment correlation coefficient in table VI. The correlation coefficient tends to increase with increasing Richardson number Ri. Similarly, at all Richardson numbers, the correlation coefficient decreases with decreasing scale or increasing scale index j. The components at the largest scale index j or smallest scale of motion are characterized by very high flatness values. This indicates strong intermittency present in the motion with the localized activity impacting the correlation coefficient. Note that with increasing Ri, the Taylor micro-scale Reynolds number Re_λ decreases. Starting from the same initial conditions, an increase of the Richardson number Ri necessarily results in the decrease of the Taylor micro-scale Reynolds number Re_λ due to the effect of stratification. Hence it is difficult to determine if the origin of the increased intermittency is due to the increased stratification or decreased Re_λ as the two effects are linked.

C. Lagrangian and Eulerian Time-Rates of Change of Fluctuating Density

The time-rates of change of fluctuating density can also be defined using Lagrangian and Eulerian approaches as

$$s_L = \frac{\partial \rho}{\partial t} + \boldsymbol{u} \cdot \nabla \rho \quad \text{and} \quad s_E = \frac{\partial \rho}{\partial t}, \tag{20}$$

respectively.

Figure 9 (top) shows the pdfs of the Lagrangian time-rate of change of fluctuating density (left) and of the corresponding Eulerian time-rate of change (right). The difference in the pdfs of the time-rates of change is well more pronounced than the difference obtained for the accelerations. Figure 9 (bottom) shows the normalized pdfs of the two time-rates of change. While the shape of the Eulerian time-rate of change pdf is again found to be stretched-exponential, the Lagrangian time-rate of change pdf has a more Gaussian shape. The extreme values of the Eulerian time-rate of change of fluctuating density are substantially larger than those of the Lagrangian time-rate of change.

Tables II and III, respectively, provide the dependence of the magnitudes of the Lagrangian and Eulerian time-rates of change on the Richardson number Ri. Note that for $Ri = 0$, the density is a passive scalar (zero gravity) with a mean gradient. Again, the magnitude of s_E always remains larger than the magnitude of s_L, consistent with the findings for the accelerations.

The flatness of the Lagrangian and Eulerian time-rates of change are also given in tables II and III, respectively. The flatness of s_E is always larger than that of s_L and their values generally decrease with increasing Ri. For strong stratification, the flatness of the Lagrangian time-rate of change assumes values around three for $Ri = 1$, while the Eulerian time-rate of change yields a value of 5.475.

Figure 10 shows pdfs of the buoyancy term (left) and advection term (right) in the advection-diffusion equation for fluctuating density. The buoyancy term pdf has a Gaussian shape as it is linearly related to the fluctuating density. Its variance increases with increasing Ri, because the stratification rate S_ρ increases. The more Gaussian shape of the Lagrangian time-rate of change of fluctuating density can be explained by the lack of a quadratic term in the advection-diffusion equation for fluctuating density. The large difference observed between the Lagrangian and Eulerian time-rates of change of fluctuating density is due to the advection term.

IV. CONCLUSIONS

A series of direct numerical simulations was performed in order to study the Lagrangian and Eulerian acceleration properties in stably stratified turbulent shear flows. With increasing Richardson number Ri, the evolution of the turbulent kinetic energy K changes from growth to decay and the variances of the Lagrangian acceleration $\boldsymbol{a}_L$ and the Eulerian acceleration $\boldsymbol{a}_E$ decrease. The acceleration pdfs were observed to have a stretched-exponential symmetric shape and the flatness decreases with increasing Ri.

We studied the cancellation of Eulerian and convective accelerations of fluid particle using geometrical statistics of the vector quantities. We found a strong preference for the anti-alignment of both vectors, which decreases with the Richardson number. This cancellation explains why the variance of the Lagrangian acceleration is smaller than its Eulerian counterpart and it supports, according to Tsinober *et al.* [1], who performed similar analyses for isotropic turbulence, the random Taylor hypothesis for shear flow which becomes however weaker with increasing stratification. Nevertheless, we do not find an order of magnitude difference in the acceleration variances, as predicted by Tennekes [11] for isotropic turbulence and necessary so that the random Taylor hypothesis strictly holds. These findings are in agreement with Lin [12], who showed that Taylor's hypothesis does in general not hold for

shear flow. Analyzing the alignment properties of the scale-dependent contributions of the acceleration is an interesting perspective for future work, already in the context of isotropic turbulence. This would allow to check if the hypothesis holds for shear flows at least as small scales.

An estimation of the variances of the Lagrangian and Eulerian accelerations has been derived from the Navier–Stokes equations which requires the ratio of potential to kinetic energy. A comparison of the estimation with results from the direct numerical simulations showed good agreement for the considered range of Richardson numbers.

The pdfs of the pressure-gradient and advection terms in the Navier–Stokes equation, which are both quadratic terms, also have stretched-exponential shapes. The Lagrangian and Eulerian accelerations are mainly determined by the pressure-gradient and advection terms, respectively. While the quadratic terms are dominant for small Ri, their dominance is somewhat diminished for large Ri. The pdfs of the shear and buoyancy terms in the Navier–Stokes equation, which are both linear terms, were observed to have a Gaussian shape. While the variance of the shear term decreases with Ri, the variance of the buoyancy term increases with Ri.

In addition, the Lagrangian and Eulerian time-rates of change of fluctuating density and of fluctuating vorticity (see appendix A) were considered. For both quantities, the Eulerian time-rates of change showed substantially larger extreme values than their Lagrangian counterparts. Due to a lack of a quadratic term on the right-hand-side of the advection-diffusion equation for fluctuating density, the pdf of the Lagrangian time-rate of change has an almost Gaussian shape, while the pdf of the Eulerian time-rate of change was observed to have exponential to stretched-exponential shapes. For fluctuating vorticity we found that the Lagrangian time-rate of change is mainly determined by the vortex streching and tilting term.

A scale-dependent analysis using orthogonal wavelet decomposition provided insight into the intermittency of the Lagrangian and Eulerian accelerations. At small scales of the turbulent motion, the pdfs exhibit heavy tails, resulting in very large flatness values and corresponding intermittency. The correlation between the Lagrangian and Eulerian accelerations has likewise been analyzed and we found stronger correlation at large scales of turbulent motion as well as with increasing Richardson number. At small scales this correlation is substantially reduced.

For rotating and sheared homogeneous turbulence, Salhi *et al.* [28] observed a dominance of linear terms in the cases with strong rotation and the flatness of the Lagrangian acceleration assumes a value of about 3. This observation suggests that linear theory can accurately describe properties of such flows. In the present study, however, the flatness never reaches values close to three, even for very large Richardson numbers. Hence, linear theory should not yield agreement with direct numerical simulation results. Indeed, Hanazaki and Hunt [23] found important differences between linear theory and the fully nonlinear evolution of homogeneous turbulence in stratified shear flows.

Perspectives for future work include a component-wise analysis of the Lagrangian and Eulerian acceleration, a more detailed scale-wise decomposition of the geometric properties of the accelerations, and corresponding terms for the vorticity evolution.

ACKNOWLEDGMENTS

FGJ acknowledges the support from a University Professor Award from the University of San Diego and the hospitality at Aix-Marseille Université. KS acknowledges financial support from Agence Nationale de la Recherche, project AIFIT (ANR-15-CE40-0019) and project CM2E (ANR-20-CE46-0010-01), and the French Research Federation for Fusion Studies within the framework of the European Fusion Development Agreement (EFDA).

Appendix A: Lagrangian and Eulerian Time-Rates of Change of Fluctuating Vorticity

The Lagrangian and Eulerian time-rates of change of fluctuating vorticity $\boldsymbol{\omega}$ are defined as

$$\boldsymbol{c}_L = \frac{\partial \boldsymbol{\omega}}{\partial t} + \boldsymbol{u} \cdot \nabla \boldsymbol{\omega} \quad \text{and} \quad \boldsymbol{c}_E = \frac{\partial \boldsymbol{\omega}}{\partial t}, \tag{A1}$$

respectively. This definition is analogous to the definition for the Lagrangian and Eulerian accelerations in order to enable a comparison between the accelerations and vorticity time-rate of change statistics. Again, the analysis is performed at the nondimensional time $St = 10$.

Figure 11 (top) shows the probability distribution functions (pdfs) of the Lagrangian time-rate of change $\boldsymbol{c}_L$ (left) and of the Eulerian time-rate of change $\boldsymbol{c}_E$ (right). Similar to

the accelerations, pdfs with stretched-exponential shapes are observed for both time-rates of change and a strong and similar influence on the Richardson number Ri is obtained. Again, stronger extreme values are obtained for the Eulerian time-rate of change, but the difference to the Lagrangian time rate of change is much more pronounced here as compared to the accelerations. Figure 11 (bottom) shows the normalized pdfs of the two time-rates of change. Again, for a core region of about five standard deviations, both the Lagrangian and Eulerian time-rates of change have an approximately similar shape. For small Richardson numbers Ri, the tails of the Lagrangian time-rate of change are heavier than those of their Eulerian counterparts. However, this ordering is reversed at larger Ri.

The magnitudes of the Lagrangian and Eulerian vorticity time-rates of change are given in tables II and III, respectively. Similar to the magnitudes of the accelerations, the magnitudes of both time-rates of change decrease with increasing Ri and the variance of $\boldsymbol{c}_E$ remains always larger than the variance of $\boldsymbol{c}_L$. This difference in the magnitudes for the vorticity time-rate of change pdfs is much more pronounced than that of the accelerations. The heavier tails observed for the pdf of $\boldsymbol{c}_L$ as compared to $\boldsymbol{c}_E$ at small Ri results in a larger flatness of the Lagrangian time-rate of change pdf as compared to its Eulerian counterpart. Again, the ordering of the flatness values is reversed at larger Ri. While the flatness values decrease with increasing Ri, the flatness is again observed to level off at a value of approximately 5, well above the value of 3 expected for a Gaussian pdf. Hence, some nonlinearity is still present even in the case of strongly suppressed turbulence in strongly stratified flows.

Figure 12 shows pdfs of the shear term (top, left), the buoyancy term (top, right), the vortex tilting and stretching term (bottom, left), and the advection term (bottom, right) in the vorticity equation. The shear and buoyancy terms depend linearly on the curl of fluctuating velocity components and fluctuating density, respectively. Similarly to the respective terms in the Navier–Stokes equation, the magnitude of the shear term decreases with increasing Ri and the magnitude of the buoyancy term increases. The pdfs of the vortex tilting and stretching term and the advection term show stretched-exponential shapes due to the quadratic nature of the terms. The magnitudes of both terms decrease with increasing Ri. For small Ri, the vortex tilting and stretching term as well as the advection term clearly dominate the shear and buoyancy terms, but this dominance again is reduced for large Ri. In the case of vorticity, the vortex tilting and stretching term is the generally dominant contribution to the Lagrangian time-rate of change, while the advection term is

important for the Eulerian time-rate of change.

Appendix B: Lagrangian and Eulerian component pdfs

While the main manuscript exclusively discusses the properties of vector pdfs, this appendix presents component pdfs of the Lagrangian and Eulerian accelerations in order to address their anisotropy in turbulent stratified shear flow. Figure 13 compares the vector pdfs with their $x-$, $y-$, and $z-$component pdfs for the Lagrangian acceleration (left) and Eulerian acceleration (right) for two cases with weak stratification with $Ri = 0.1$ (top) and with strong stratification with $Ri = 1$ (bottom). All pdfs show similar shapes and the flow anisotropy is reflected in the variances. A similar observation holds for the pdfs of Lagrangian and Eulerian time-rate of change of fluctuating vorticity (not shown here).

The ratios of the component variances to the corresponding vector variances of the Lagrangian and Eulerian accelerations are given in tables II and III, respectively. For small Richardson numbers Ri, the variance ratios show an almost equipartition between the three components for both the Lagrangian and Eulerian accelerations. For large Ri, however, the ratio of the vertical variances to the vector variances gains due to the direct impact of the buoyancy term in the vertical component of the Navier–Stokes equation. Figure 2 shows that the ratio of potential to kinetic energy increases with increasing Ri. Hence the buoyancy term impacts particularly the vertical component of the accelerations.

---

[1] A. Tsinober, P. Vedula, and P.K. Yeung, "Random Taylor hypothesis and the behavior of local and convective accelerations in isotropic turbulence," Phys. Fluids **13**, 1974–1984 (2001).

[2] A. Tsinober, *An informal introduction to turbulence* (Kluwer Academic Publishers, 2001).

[3] W. Heisenberg, "Zur statistischen Theorie der Turbulenz," Zeitschrift für Physik **124**, 628–657 (1948).

[4] A. M. Yaglom, "On the acceleration field in a turbulent flow," C.R. Akad. URSS **67**, 795–798 (1949).

[5] S. B. Pope, "Lagrangian pdf methods for turbulent flows," Annu. Rev. Fluid Mech. **26**, 23–63 (1994).

[6] A. La Porta, G. A. Voth, A. M. Crawford, J. Alexander, and E. Bodenschatz, "Fluid particle accelerations in fully developed turbulence," Nature **409**, 1017 (2001).

[7] P. K. Yeung and S.B. Pope, "Lagrangian statistics from direct numerical simulations of isotropic turbulence," J. Fluid Mech. **207**, 531–586 (1989).

[8] P. K. Yeung, "Lagrangian investigations of turbulence," Annu. Rev. Fluid Mech. **34**, 115 (2002).

[9] F. Toschi and E. Bodenschatz, "Lagrangian properties of particles in turbulence," Annu. Rev. Fluid Mech. **41**, 375 (2009).

[10] M. Pinsky, A. Khain, and A. Tsinober, "Accelerations in isotropic and homogeneous turbulence and Taylor's hypothesis," Phys. Fluids **12**, 3195–3204 (2000).

[11] H. Tennekes, "Eulerian and Lagrangian time microscales in isotropic turbulence," J. Fluid Mech. **67**, 561–567 (1975).

[12] C. C. Lin, "On Taylor's hypothesis and the acceleration terms in the Navier-Stokes equation," Quarterly of Applied Mathematics **10**, 295–306 (1953).

[13] G. He, G. Jin, and Y. Yang, "Space-time correlations and dynamic coupling in turbulent flows," Annu. Rev. Fluid Mech. **49**, 51–70 (2017).

[14] S. Komori, H. Ueda, F. Ogino, and T. Mizushina, "Turbulence structure in stably stratified open-channel flow," J. Fluid Mech. **130**, 13–26 (1983).

[15] J. J. Rohr, E. C. Itsweire, K. N. Helland, and C. W. Van Atta, "Growth and decay of turbulence in a stably stratified shear flow," J. Fluid Mech. **195**, 77–111 (1988).

[16] P. S. Piccirillo and C. W. Van Atta, "The evolution of a uniformly sheared thermally stratified turbulent flow," J. Fluid Mech. **334**, 61–86 (1997).

[17] K. H. Keller and C. W. Van Atta, "An experimental investigation of the vertical temperature structure of homogeneous stratified shear turbulence," J. Fluid Mech. **425**, 1–29 (2000).

[18] T. Gerz, U. Schumann, and S. E. Elghobashi, "Direct numerical simulation of stratified homogeneous turbulent shear flows," J. Fluid Mech. **200**, 563–594 (1989).

[19] S. E. Holt, J. R. Koseff, and J. H. Ferziger, "A numerical study of the evolution and structure of homogeneous stably stratified sheared turbulence," J. Fluid Mech. **237**, 499–539 (1992).

[20] F. G. Jacobitz, S. Sarkar, and C. W. Van Atta, "Direct numerical simulations of the turbulence evolution in a uniformly sheared and stably stratified flow," J. Fluid Mech. **342**, 231–261 (1997).

[21] F. G. Jacobitz, "A comparison of the turbulence evolution in a stratified fluid with vertical or horizontal shear," J. Turbul. **3**, 1–16 (2002).

[22] G. D. Portwood, *A Study on Homogeneous Sheared Stably Stratified Turbulence*, Ph.D. thesis, University of Massachusetts, Amherst, Amherst, MA (2019).

[23] H. Hanazaki and J. C. R. Hunt, "Structure of unsteady stably stratified turbulence with mean shear," J. Fluid Mech. **507**, 1–42 (2004).

[24] H. Salehipour, W. R. Peltier, and A. Mashayek, "Turbulent diapycnal mixing in stratified shear flows: the influence of Prandtl number on mixing efficiency and transition at high reynolds number," J. Fluid Mech. **773**, 178–223 (2015).

[25] S. K. Venayagamoorthy and J. R. Koseff, "On the flux richardson number in stably stratified turbulence," J. Fluid Mech. **798**, R1 (2016).

[26] M. C. Gregg, E. A. D'Asaro, J. J. Riley, and E. Kunze, "Mixing efficiency in the ocean," Annu. Rev. Mar. Sci. **10**, 443–473 (2018).

[27] F. G. Jacobitz, K. Schneider, W. J. T. Bos, and M. Farge, "Structure of sheared and rotating turbulence: Multiscale statistics of Lagrangian and Eulerian accelerations and passive scalar dynamics," Phys. Rev. E **93**, 013113 (2016).

[28] A. Salhi, F. G. Jacobitz, K. Schneider, and C. Cambon, "Nonlinear dynamics and anisotropic structure of rotating sheared turbulence," Phys. Rev. E **89**, 013020 (2014).

[29] R. S. Rogallo, *Numerical experiments in homogeneous turbulence*, Technical Report TM 81315 (NASA Ames Research Center, Moffett Field, CA, United States, 1981).

[30] T. Hou and R. Li, "Computing nearly singular solutions using pseudo-spectral methods," J. Comput. Phys. **226**, 379–397 (2007).

[31] S. Mallat, *A Wavelet Tour of Signal Processing* (Academic Press, 1998).

[32] M. Farge and K. Schneider, "Wavelet transforms and their applications to MHD and plasma turbulence: a review," J. Plasma Phys. **81**, 435810602 (2015).

[33] K. Schneider, M. Farge, and N. Kevlahan, "Spatial intermittency in two–dimensional turbulence: a wavelet approach," in *Woods Hole Mathematics, Perspectives in Mathematics and Physics*, Vol. 34, edited by N. Tongring and R.C. Penner (World Scientific, 2004) pp. 302–328.

[34] A. S. Monin and A. M. Yaglom, *Statistical Fluid Mechanics: The Mechanics of Turbulence*, Vol. I (M.I.T. Press, 1971).

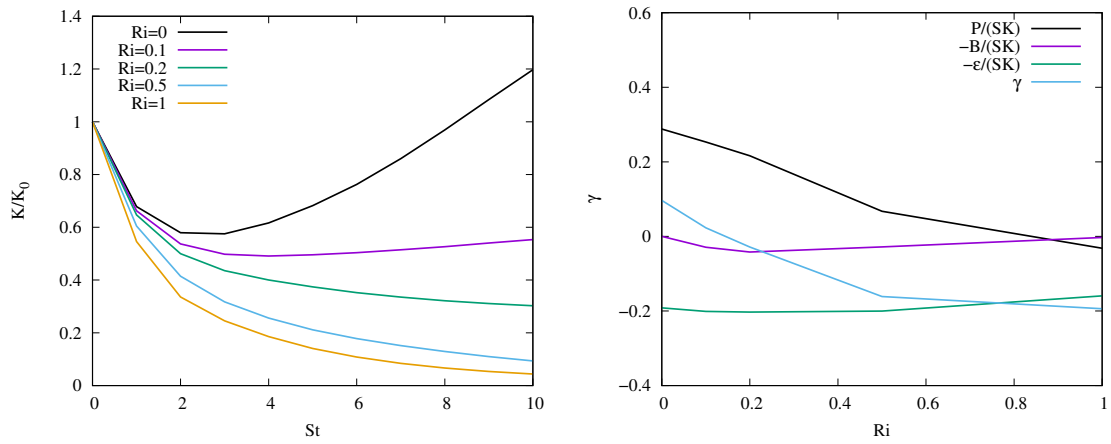

FIG. 1. Evolution of the turbulent kinetic energy K in nondimensional time St (left) and dependence of the normalized production rate $P/(SK)$, buoyancy flux $B/(SK)$, and dissipation rate $\epsilon/(SK)$ on the Richardson number at $St = 10$ (right).

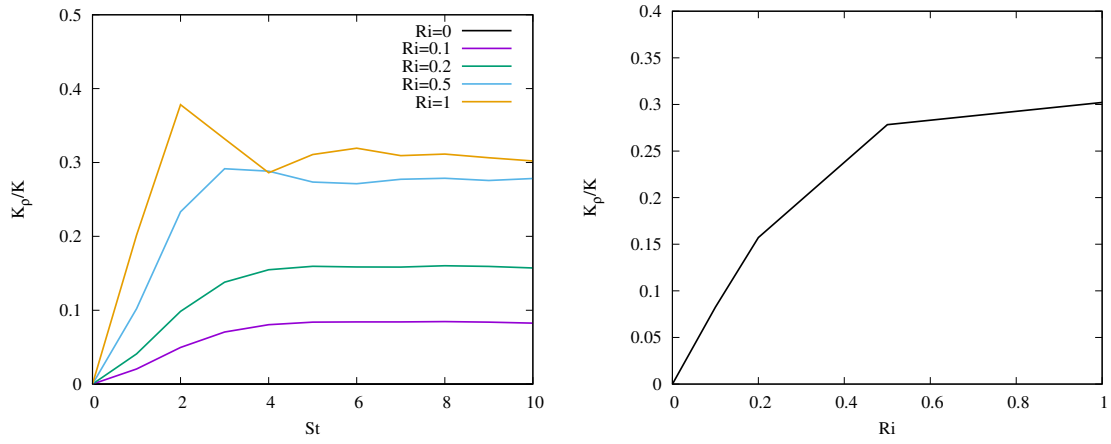

FIG. 2. Evolution of the ratio of turbulent potential to kinetic energy K_ρ/K in nondimensional time St (left) and dependence of this ratio on the Richardson number at $St = 10$ (right).

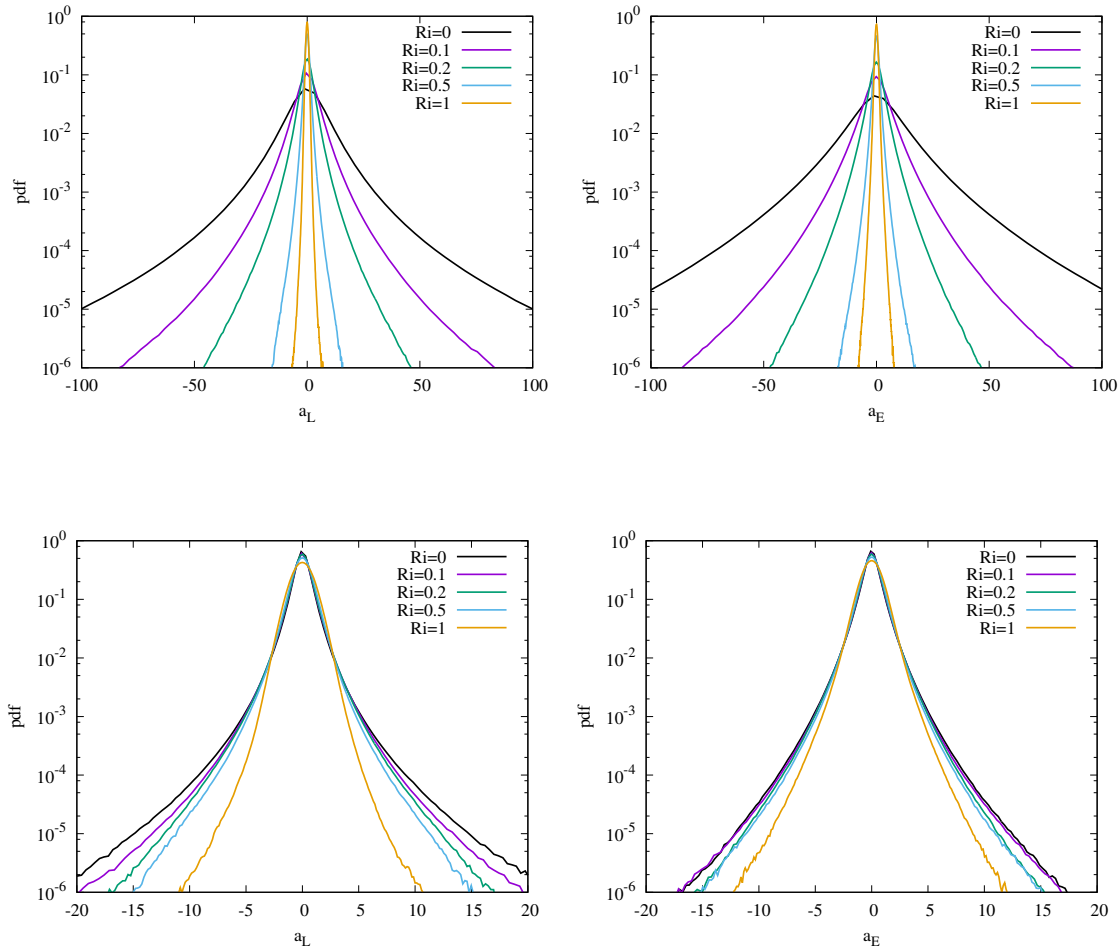

FIG. 3. Pdfs (top) and pdfs normalized with the corresponding standard deviations (bottom) of Lagrangian acceleration $\boldsymbol{a}_L$ (left) and Eulerian acceleration $\boldsymbol{a}_E$ (right) at nondimensional time $St = 10$. Note that all pdfs are estimated using histograms with 100 bins, and they are plotted in log-lin representation. Note that pdfs for the vector quantities are shown.

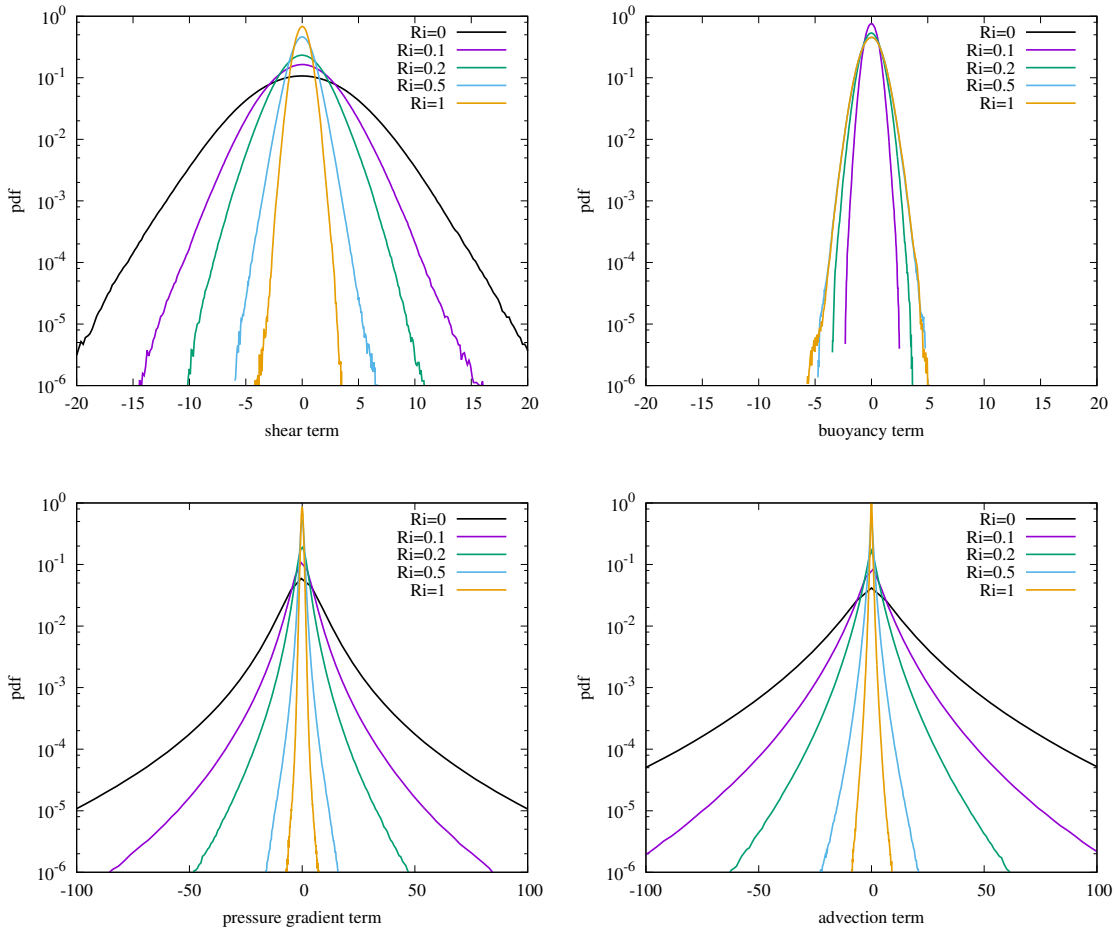

FIG. 4. Pdfs of the shear (top, left), buoyancy (top, right), pressure-gradient (bottom, left), and advection (bottom, right) terms in the Navier–Stokes equations at nondimensional time $St = 10$.

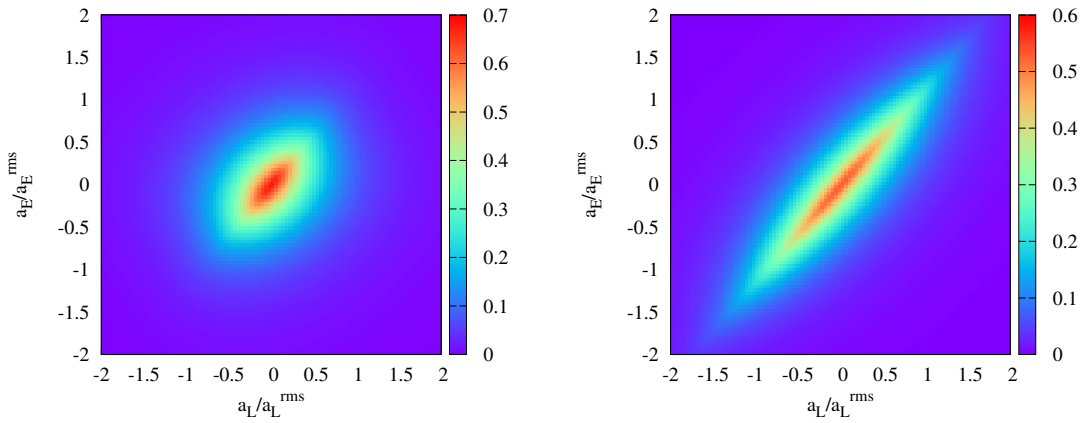

FIG. 5. Joint pdfs of Lagrangian acceleration $\boldsymbol{a}_L$ and Eulerian acceleration $\boldsymbol{a}_E$ for Richardson numbers $Ri = 0.1$ (left) and $Ri = 1$ (right) at nondimensional time $St = 10$ using a linear color scale.

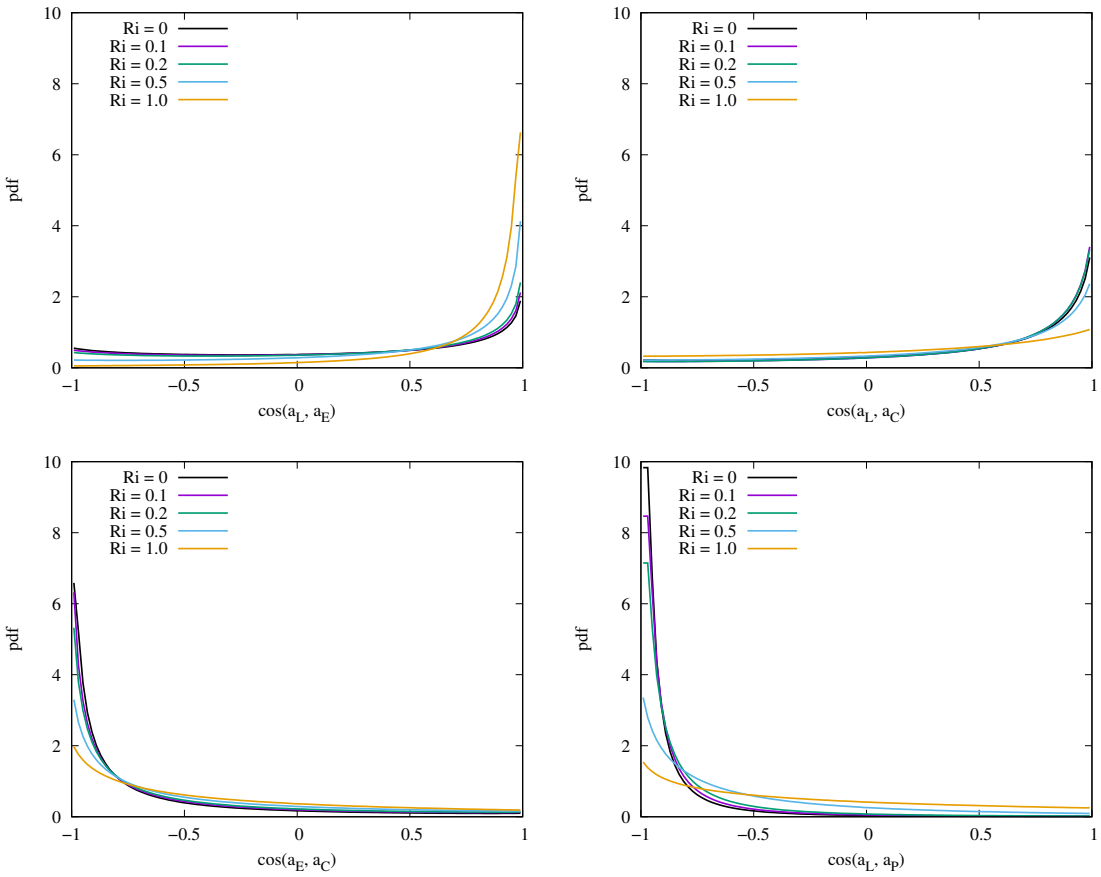

FIG. 6. Pdfs of the cosine of the angles between different acceleration contributions: $\cos(a_L, a_E)$ (top, left), $\cos(a_L, a_C)$ (top, right), $\cos(a_E, a_C)$ (bottom, left), and $\cos(a_L, a_P)$ (bottom, right) for different Ri at nondimensional time $St = 10$.

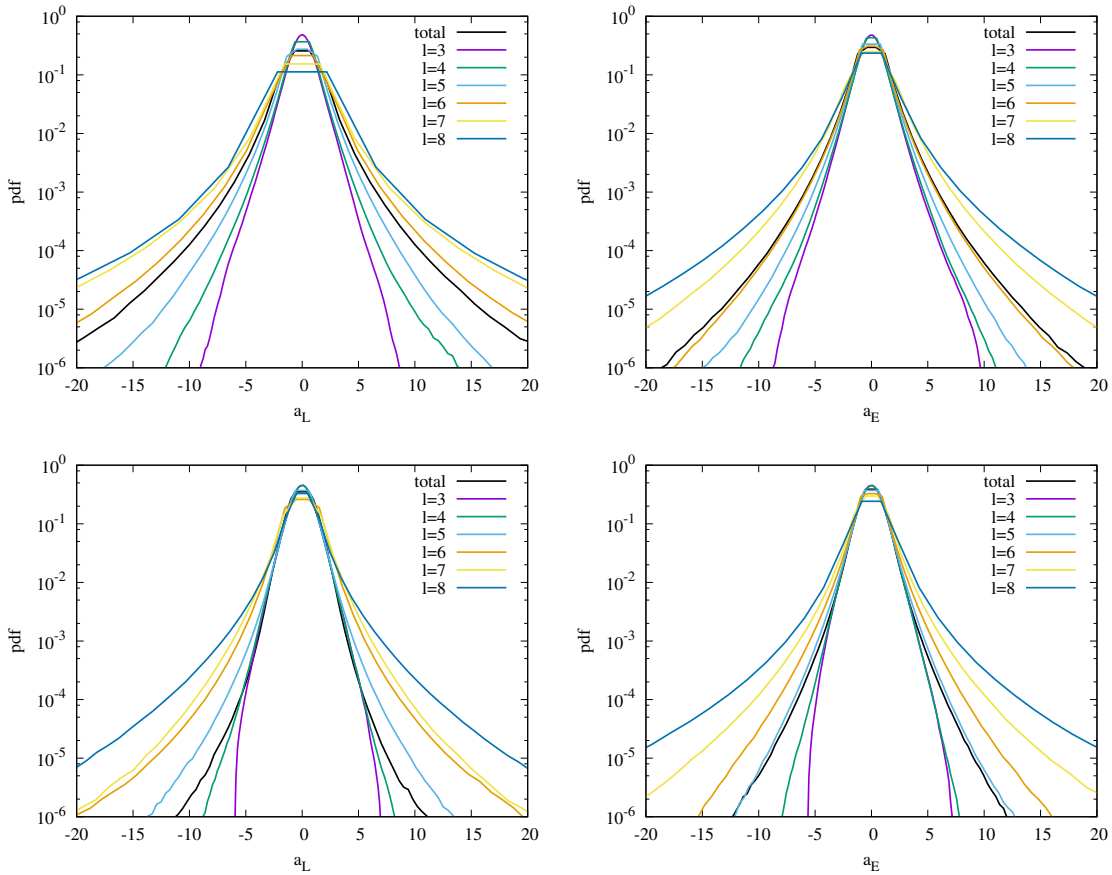

FIG. 7. Scale-dependent normalized pdfs of Lagrangian acceleration $\boldsymbol{a}_L$ (left) and Eulerian acceleration $\boldsymbol{a}_E$ (right) for Richardson numbers $Ri = 0.1$ (top) and $Ri = 1$ (bottom) at nondimensional time $St = 10$. Note that the flat sections in the pdfs around zero are artifacts of an even number of bins chosen in the computation of the pdfs. Additionally, pdfs of quantities with large variances only show fewer bins in the figure.

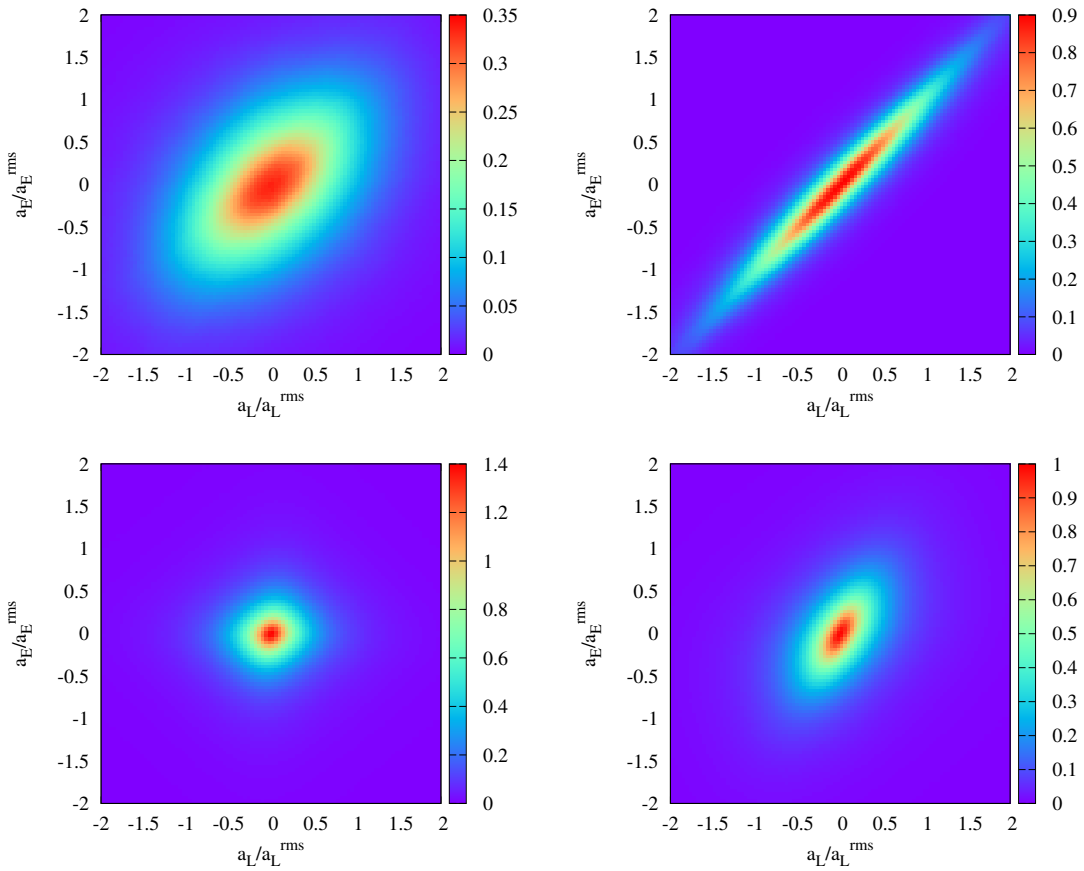

FIG. 8. Scale-dependent joint pdfs of Lagrangian acceleration $\boldsymbol{a}_L$ and Eulerian acceleration $\boldsymbol{a}_E$ for Richardson numbers $Ri = 0.1$ (left) and $Ri = 1$ (right) and at large scale with scale index $j = 3$ (top) and at small scale with $j = 7$ (bottom) at nondimensional time $St = 10$ using a linear color scale.

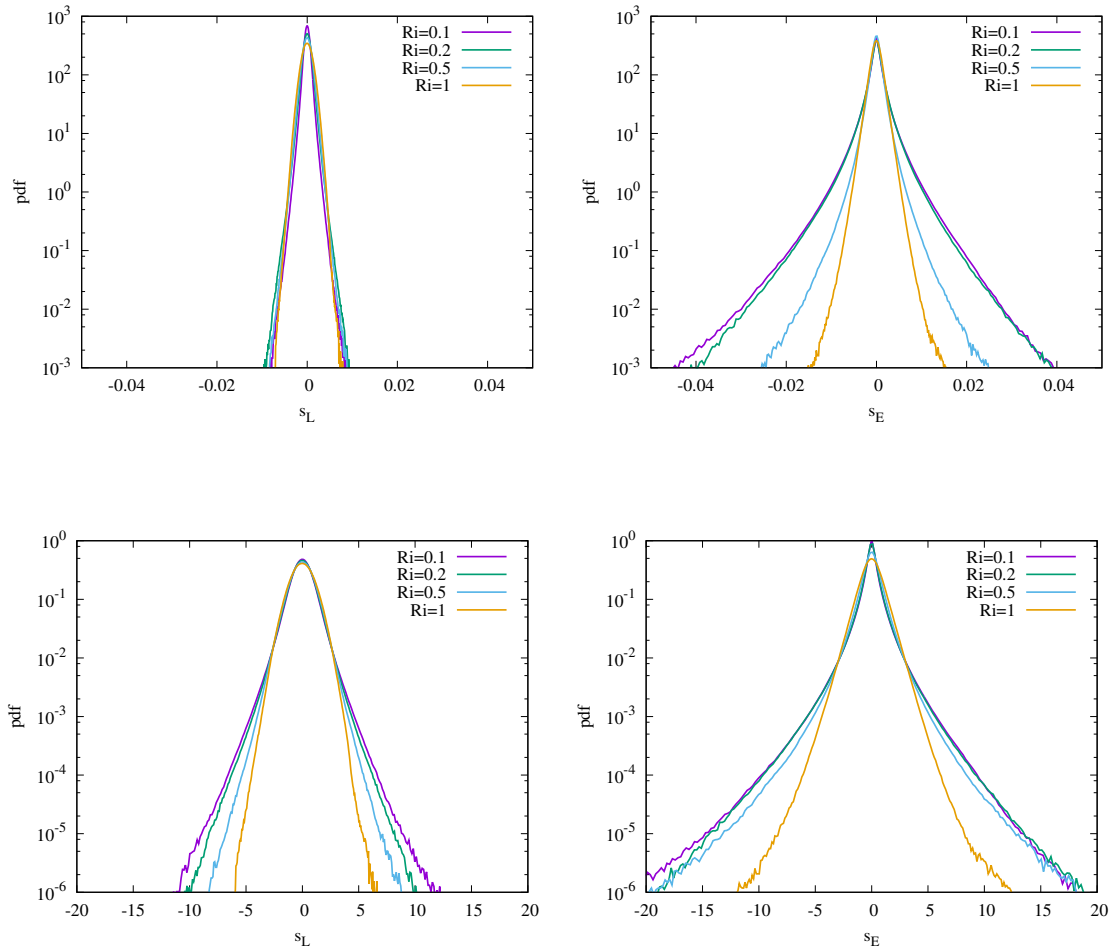

FIG. 9. Pdfs (top) and normalized pdfs (bottom) of Lagrangian time-rate of change of fluctuating density s_L (left) and Eulerian time-rate of change s_E (right) at nondimensional time $St = 10$.

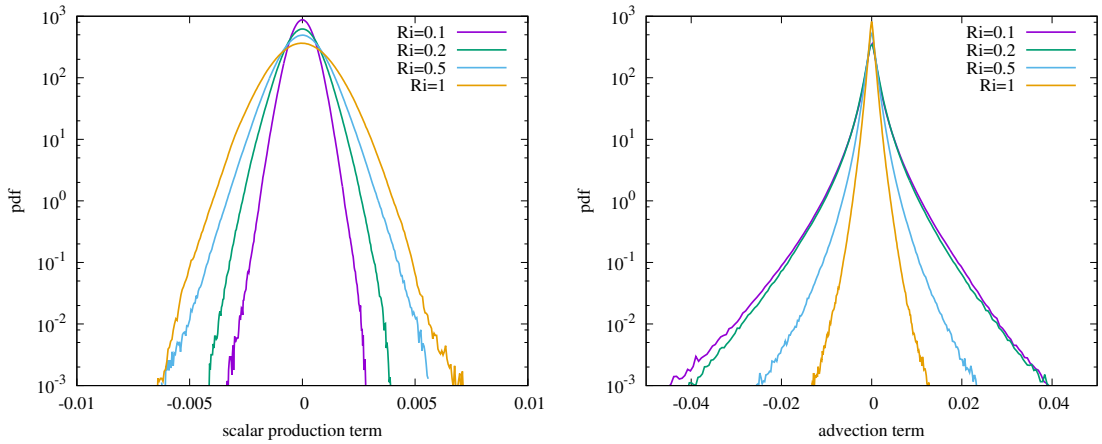

FIG. 10. Pdfs of the buoyancy (left) and advection (right) terms in the advection-diffusion equation for fluctuating density at nondimensional time $St = 10$.

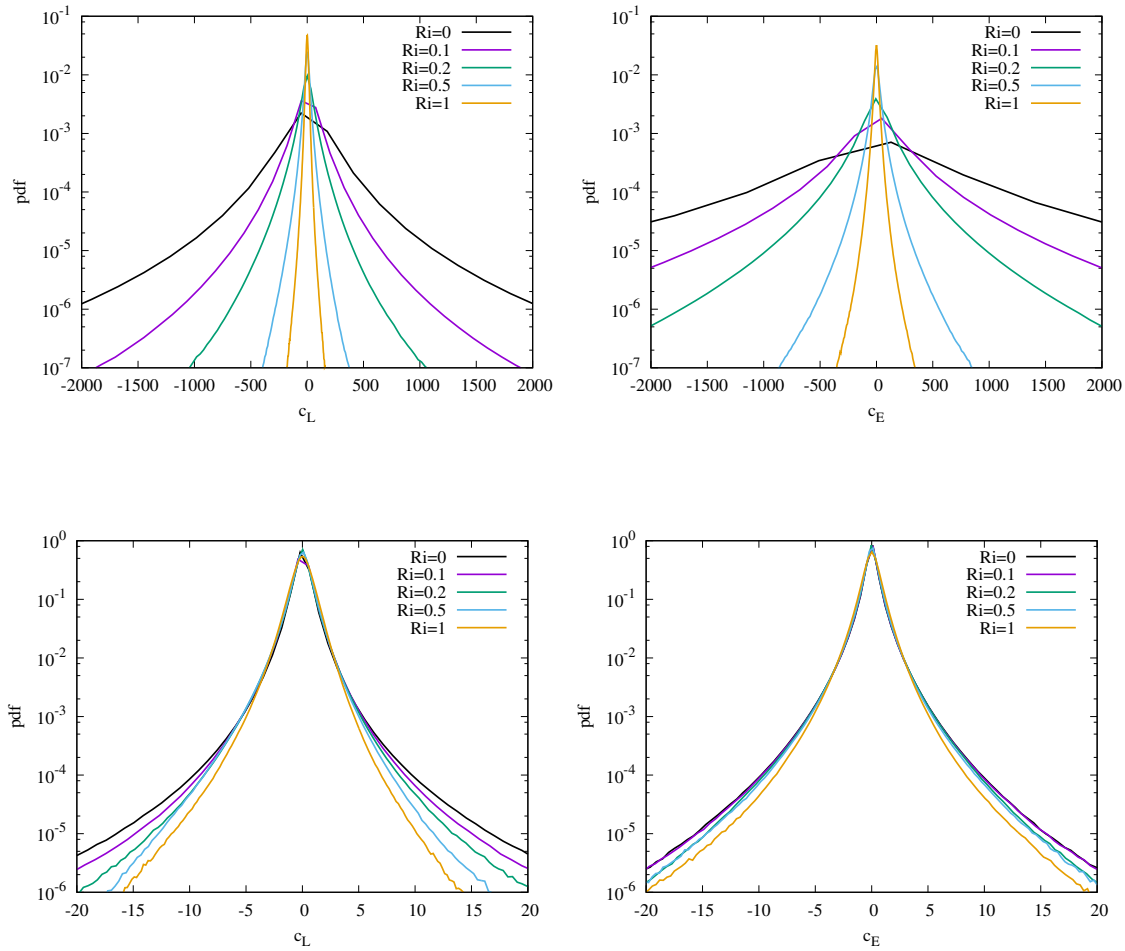

FIG. 11. Pdfs (top) and normalized pdfs (bottom) of Lagrangian time-rate of change of vorticity c_L (left) and Eulerian time-rate of change c_E (right) at nondimensional time $St = 10$. Note that pdfs for the vector quantities are shown.

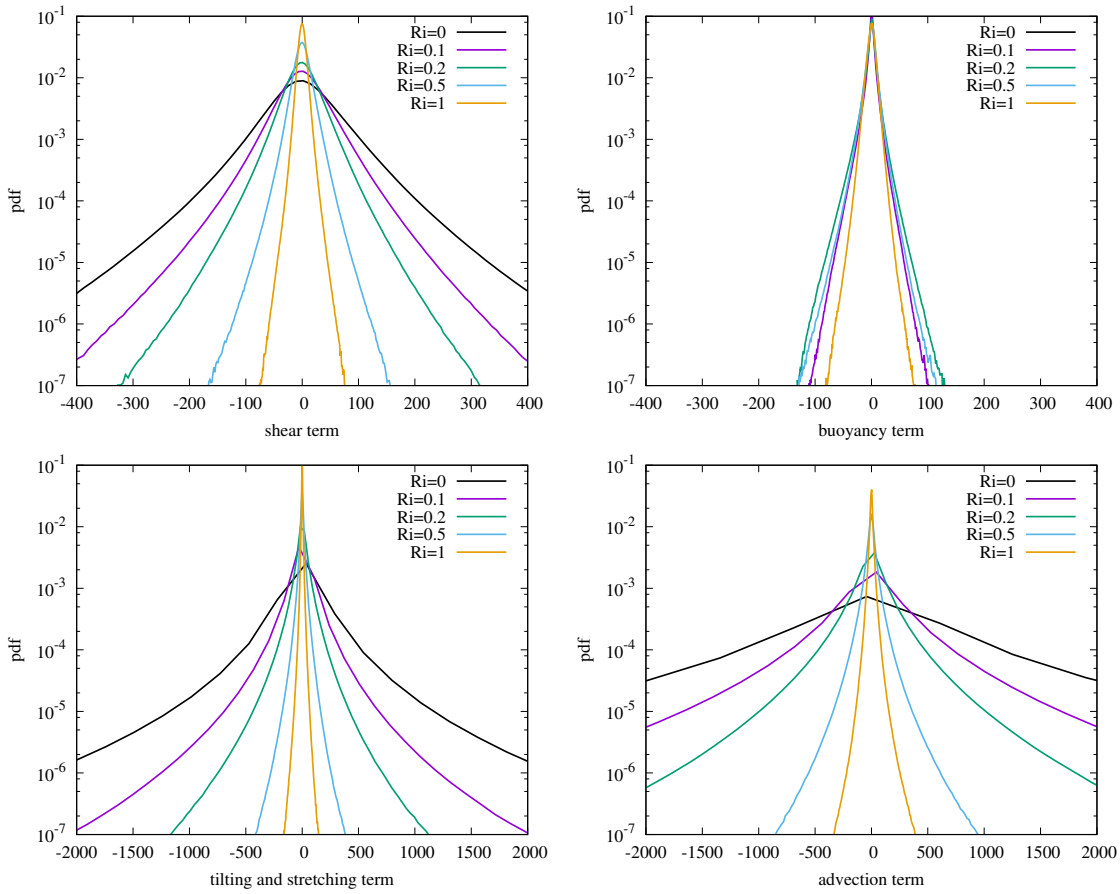

FIG. 12. Pdfs of the shear (top, left), buoyancy (top, right), vortex tilting and stretching (bottom, left), and advection (bottom, right) terms in the vorticity equation at nondimensional time $St = 10$.

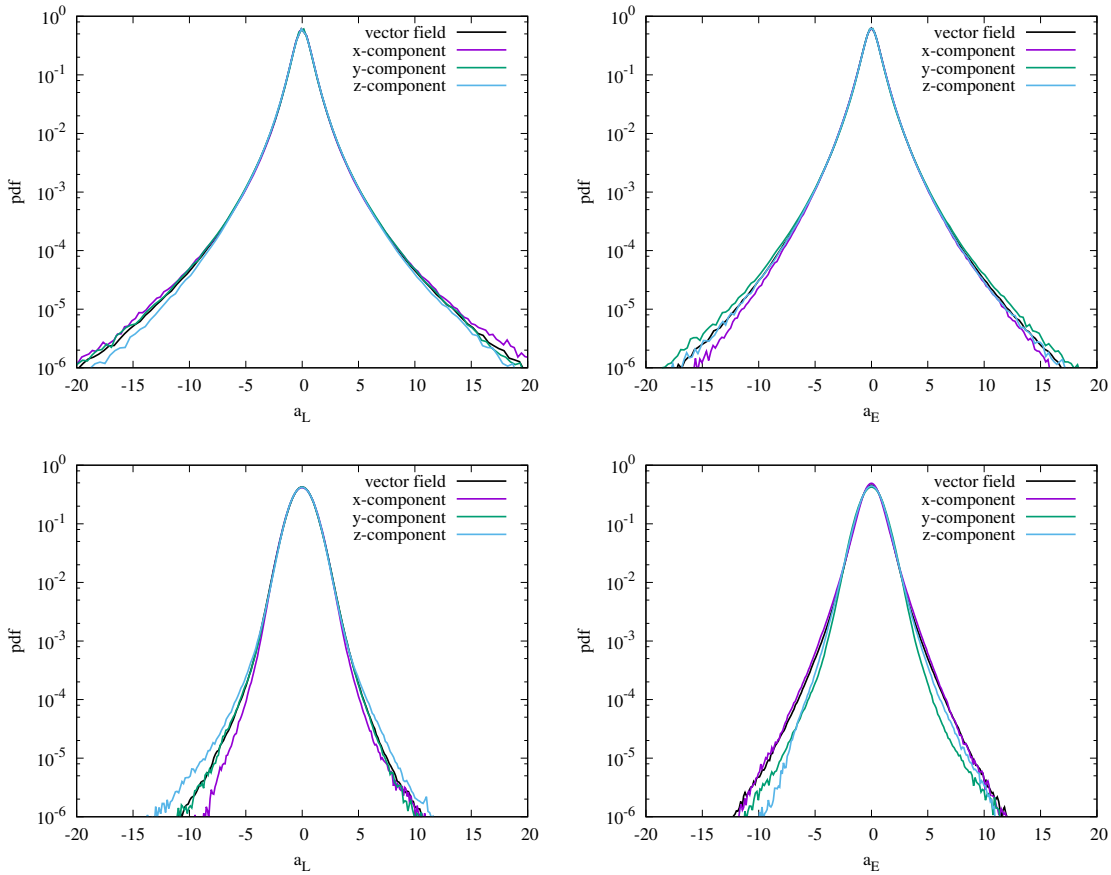

FIG. 13. Comparison of normalized vector pdfs with their corresponding normalized component pdfs for Lagrangian acceleration (left) and Eulerian acceleration (right) for $Ri = 0.1$ (top) and $Ri = 1$ (bottom) at nondimensional time $St = 10$.

TABLE I. Overview of the simulation cases, including the Richardson number Ri, the shear rate S, the Brunt–Väisälä frequency N, the Taylor-micro scale Reynolds number Re_λ, The viscosity ν, the turbulent velocity fluctuation q, the dissipation rate of kinetic energy ϵ, the cut-off wavenumber $k_{max}\eta$, the overturning scale $L_{overturn}$, the Ellison scale $L_{Ellison}$, the Ozmidov scale $L_{Ozmidov}$, the Taylor microscale λ, and the Kolmogorov scale η. All values are given at nondimensional time $St = 10$. All symbols are defined in the text.

Ri	0	0.1	0.2	0.5	1
S	5.3345	5.3345	5.3345	5.3345	5.3345
N	0.0000	1.6869	2.3856	3.7720	5.3345
Re_λ	156.90	104.08	76.60	42.84	32.83
ν	0.0010	0.0010	0.0010	0.0010	0.0010
q	1.5856	1.0779	0.7969	0.4428	0.3028
ϵ	1.2838	0.6230	0.3436	0.1048	0.0390
$k_{max}\eta$	1.1992	1.4368	1.6673	2.2437	2.8723
$L_{overturn}$	3.1052	2.0101	1.4728	0.8288	0.7119
$L_{Ellison}$	0.2619	0.1835	0.1324	0.0619	0.0312
$L_{Ozmidov}$	N/A	0.3603	0.1591	0.0442	0.0160
λ	0.09895	0.09656	0.09613	0.09675	0.10841
η	0.00528	0.00633	0.00735	0.00988	0.01265

TABLE II. Lagrangian acceleration statistics at nondimensional time $St = 10$ showing the rms of the Lagrangian acceleration a_L, the flatness Fl_{a_L} and the ratio of the component-wise variances and the total variance. The variance and flatness values of the time-rates of change of fluctuating density s_L and Fl_{s_L} and fluctuating vorticity c_L and Fl_{c_L} are likewise given.

Ri	0	0.1	0.2	0.5	1
a_L	19.427	9.833	5.519	1.808	0.942
Fl_{a_L}	27.814	26.041	13.115	9.364	4.111
a_{Lx}^2/a_L^2	0.335	0.318	0.306	0.320	0.327
a_{Ly}^2/a_L^2	0.325	0.327	0.331	0.356	0.390
a_{Lz}^2/a_L^2	0.340	0.355	0.363	0.324	0.242
s_L	0.00117	0.00070	0.00091	0.00101	0.00119
Fl_{s_L}	7.220	6.148	5.152	3.989	3.249
c_L	490.484	232.508	128.472	44.395	19.725
Fl_{c_L}	65.574	53.766	21.168	14.123	9.177

TABLE III. Eulerian acceleration statistics at nondimensional time $St = 10$ showing the rms of the Eulerian acceleration a_E, the flatness Fl_{a_E} and the ratio of the component-wise variances and the total variance. The variance and flatness values of the time-rates of change fluctuating density s_E and Fl_{s_E} and of fluctuating vorticity c_E and Fl_{c_E} are likewise given.

Ri	0	0.1	0.2.	0.5.	1
a_E	26.100	11.689	6.258	1.975	1.075
Fl_{a_E}	14.414	13.413	11.028	9.510	5.691
a_{Ex}^2/a_E^2	0.302	0.320	0.339	0.408	0.434
a_{Ey}^2/a_E^2	0.329	0.312	0.292	0.261	0.273
a_{Ez}^2/a_E^2	0.369	0.368	0.369	0.331	0.293
s_E	0.00577	0.00239	0.00231	0.00138	0.00129
Fl_{s_E}	24.992	24.624	21.960	16.053	5.475
c_E	2,020.203	781.238	372.030	91.830	34.461
Fl_{c_E}	37.813	35.619	27.855	24.893	17.724

TABLE IV. Variance of the contributions to the linear term from the shear term Λ_S^2, the buoyancy term Λ_B^2, and viscous term Λ_V^2, an estimate for the variance of the linear term using the triangle inequality Λ_{DNS}^2, the variance of the velocity q^2, the ratio of potential to kinetic energies K_ρ/K, and an estimate for the linear term Λ^2 given in equation 14 at nondimensional time $St = 10$.

Ri	0	0.1	0.2	0.5	1
Λ_S^2	14.5746	6.3796	3.2517	0.8430	0.3596
Λ_B^2	0.0000	0.2728	0.5681	0.7767	0.7886
Λ_V^2	6.8850	2.5158	1.1384	0.2568	0.0723
Λ_{DNS}^2	21.4596	9.1682	4.9581	1.8764	1.2205
q^2	2.5142	1.1619	0.6350	0.1961	0.0917
K_ρ/K	0.0000	0.0825	0.1571	0.2783	0.3021
Λ^2	23.8427	11.2910	6.5897	2.6358	1.6579

TABLE V. Mean value of the cosine of the angle $\overline{\cos}$ and Pearson product-moment correlation coefficient r between the Lagrangian accelerations $\boldsymbol{a}_L$, the Eulerian acceleration $\boldsymbol{a}_E$, the convective contribution $\boldsymbol{a}_C = \boldsymbol{N}$ and the pressure gradient $\boldsymbol{a}_C = \boldsymbol{\Pi}$ at nondimensional time $St = 10$. The correlation coefficient is determined for all three components of the vector fields.

Ri	0	0.1	0.2	0.5	1
$r(\boldsymbol{a}_L, \boldsymbol{a}_E)$	0.0284	0.0510	0.0882	0.2852	0.6634
$r(\boldsymbol{a}_L, \boldsymbol{a}_C)$	0.5823	0.6205	0.6232	0.5493	0.2741
$r(\boldsymbol{a}_E, \boldsymbol{a}_C)$	-0.7961	-0.7516	-0.7241	-0.6443	-0.5378
$r(\boldsymbol{a}_L, \boldsymbol{a}_P)$	-0.9728	-0.9545	-0.9211	-0.7014	-0.2843
$\overline{\cos}(\boldsymbol{a}_L, \boldsymbol{a}_E)$	0.1617	0.1957	0.2397	0.4347	0.7033
$\overline{\cos}(\boldsymbol{a}_L, \boldsymbol{a}_C)$	0.4199	0.4579	0.4582	0.3749	0.1964
$\overline{\cos}(\boldsymbol{a}_E, \boldsymbol{a}_C)$	-0.6573	-0.5945	-0.5563	-0.4561	-0.3538
$\overline{\cos}(\boldsymbol{a}_L, \boldsymbol{a}_P)$	-0.9110	-0.8761	-0.8157	-0.5273	-0.2659

TABLE VI. Pearson product-moment correlation coefficient r for the scale-dependent Lagrangian and Eulerian accelerations at nondimensional time $St = 10$. The correlation coefficient is determined for all three components of the accelerations.

Ri	0	0.1	0.2	0.5	1
r $(j = 0)$	0.8584	0.9716	0.9892	0.9969	0.9995
r $(j = 1)$	0.8065	0.9347	0.9625	0.9957	0.9990
r $(j = 2)$	0.5208	0.6709	0.8287	0.9728	0.9921
r $(j = 3)$	0.1988	0.3427	0.5072	0.8257	0.9512
r $(j = 4)$	0.0884	0.1380	0.2141	0.4959	0.7765
r $(j = 5)$	0.0308	0.0478	0.0739	0.2002	0.4528
r $(j = 6)$	0.0116	0.0196	0.0304	0.0993	0.2919
r $(j = 7)$	0.0037	0.0097	0.0248	0.1248	0.3337
r $(j = 8)$	-0.0052	0.0200	0.0261	0.1707	0.3837

TABLE VII. Scale-dependent Lagrangian and Eulerian acceleration statistics for $Ri = 0.1$ at nondimensional time $St = 10$ showing the rms of the Lagrangian and Eulerian acceleration, a_E and a_L, and the flatness, Fl_{a_E} and Fl_{a_L} for the total and the scale-dependent contributions at scale 2^{-j}.

j	total	0	1	2	3	4	5	6	7	8
a_L	9.833	0.156	0.361	0.769	1.787	3.672	5.666	5.773	3.491	1.280
Fl_{a_L}	26.041	4.933	3.468	4.706	4.968	6.844	10.979	39.138	119.480	252.821
a_E	11.689	0.150	0.360	0.682	1.589	3.477	6.026	7.137	5.344	2.364
Fl_{a_E}	13.413	4.296	3.304	4.103	5.061	5.981	8.114	12.607	27.600	65.829

TABLE VIII. Scale-dependent Lagrangian and Eulerian acceleration statistics for $Ri = 1$ at nondimensional time $St = 10$ showing the rms of the Lagrangian and Eulerian acceleration, a_E and a_L, and the flatness, Fl_{a_E} and Fl_{a_L}.

j	total	0	1	2	3	4	5	6	7	8
a_L	0.942	0.079	0.257	0.328	0.405	0.450	0.435	0.336	0.190	0.058
Fl_{a_L}	4.111	5.690	3.210	4.042	4.064	4.248	6.316	11.850	15.906	38.999
a_E	1.075	0.079	0.257	0.330	0.410	0.473	0.530	0.483	0.254	0.062
Fl_{a_E}	5.691	5.700	3.210	4.021	4.034	4.166	6.524	10.411	21.338	66.034